# Decoupled Fréchet kernels based on a fractional viscoacoustic wave equation

**Guangchi Xing*** **and Tieyuan Zhu*†**

**Department of Geosciences, The Pennsylvania State University, University Park, PA 16802* †*EMS Energy Institute, The Pennsylvania State University, University Park, PA 16802*

(October 21, 2021)

Running head: **Decoupled viscoacoustic Fréchet kernel**

## ABSTRACT

We formulate the Fréchet kernel computation using the adjoint-state method based on a fractional viscoacoustic wave equation. We first numerically prove that both the 1/2- and the 3/2-order fractional Laplacian operators are self-adjoint. Using this property, we show that the adjoint wave propagator preserves the dispersion and compensates the amplitude, while the time-reversed adjoint wave propagator behaves identically as the forward propagator with the same dispersion and dissipation characters. Without introducing rheological mechanisms, this formulation adopts an explicit $Q$ parameterization, which avoids the implicit $Q$ in the conventional viscoacoustic/viscoelastic full waveform inversion ($Q$-FWI). In addition, because of the decoupling of operators in the wave equation, the viscoacoustic Fréchet kernel is separated into three distinct contributions with clear physical meanings: lossless propagation, dispersion, and dissipation. We find that the lossless propagation kernel dominates the velocity kernel, while the dissipation kernel dominates the attenuation kernel over the dispersion kernel. After validating the Fréchet kernels using the finite-

difference method, we conduct a numerical example to demonstrate the capability of the kernels to characterize both velocity and attenuation anomalies. The kernels of different misfit measurements are presented to investigate their different sensitivities. Our results suggest that rather than the traveltime, the amplitude and the waveform kernels are more suitable to capture attenuation anomalies. These kernels lay the foundation for the multiparameter inversion with the fractional formulation, and the decoupled nature of them promotes our understanding of the significance of different physical processes in the $Q$-FWI.

# INTRODUCTION

Full waveform inversion (FWI, e.g., Virieux and Operto, 2009), as well as the more general adjoint tomography (e.g., Tromp et al., 2005), utilizes the adjoint-state method (e.g., Plessix, 2006) to minimize the misfit between observed and synthetic seismograms by iteratively adjusting the model parameters. This method has wide applications ranging from near surface imaging, to exploration-scale inversion, and to global tomography. For a broader overview, the reader can refer to the reviews on this topic (Fichtner, 2010; Liu and Gu, 2012). In FWI, the Fréchet kernel (i.e., the gradient of the objective function with respect to the model parameters) is computed by interacting the forward and the adjoint wavefields at each iteration. It provides the (opposite) direction for model parameters to update, refining a low-resolution initial model into a high-resolution final model. The accuracy of the final model depends critically on whether the modeling takes into account all the relevant wave physics (Tarantola, 1988). While the classic FWI algorithm is focused on the inversion of seismic velocity, seismic attenuation, quantified by the quality factor $Q$, plays an important role, especially in the study of both shallow and deep Earth geology having partial melt (e.g., Wiens et al., 2008), high temperature (e.g., Romanowicz, 1995), or fluid-saturated rocks (e.g., Müller et al., 2010). Physically, attenuation distorts the seismic waveform by reducing the amplitude (dissipation) and altering the phase (dispersion). Thus, to accurately account for the dissipation and the dispersion effects, it is crucial to incorporate seismic attenuation into the FWI workflow via the computation of the Fréchet kernel. In this way, the resultant velocity kernel can enhance the accuracy and reliability of the final velocity model; the attenuation kernel can lead to an additional high-resolution $Q$ model, which provides complementary constraints of subsurface structure (Zhu et al., 2013, 2017).

Nevertheless, incorporating seismic attenuation brings about complications. First, the state-of-the-art time-domain viscoacoustic/viscoelastic FWI ($Q$-FWI) algorithms represent seismic attenuation by superposing rheological mechanisms to approximate the widely accepted frequency-independent-$Q$ (also known as constant-$Q$, McDonal et al., 1958; Knopoff, 1964). As a consequence, $Q$ is usually parametrized implicitly by different relaxation times characterizing their corresponding rheological mechanisms, which brings complexity to the $Q$ inversion. Recently, Fichtner and van Driel (2014) and Yang et al. (2016) proposed a special parameterization to enforce the explicit representation of $Q$, which involves an additional curve-fitting procedure parametrizing the weight and the relaxation time of each rheological mechanism to fit the constant-$Q$; and the accuracy of $Q$ between 50 and 500 was satisfied with 3 rheological mechanisms. Second, the attenuation-associated physical processes, i.e., dissipation and dispersion, are always coupled with each other and with lossless wave propagation. This coupling complicates both forward and inversion problems, and hinders our understanding of the contribution to the Fréchet kernel (and thus to the $Q$-FWI) from each individual physical process. Bai et al. (2014) built the adjoint-based theoretical framework for viscoacoustic monoparameter (velocity) inversion; with the "unrelaxed" velocity as the model parameter, the velocity gradient (i.e., Fréchet kernel) has the same form as lossless acoustic FWI, and the input of dissipation and dispersion vanish. Fichtner and van Driel (2014) and Yang et al. (2016)'s formulations involve the forward or adjoint memory variables into the wavefield interaction to compute both velocity (or modulus) and attenuation kernels. The contributions from dissipation or dispersion process are implicitly embedded in these memory variables. Another $Q$-FWI method (Tromp et al., 2005) obtains the attenuation kernel with an additional adjoint simulation excited by a $Q$ adjoint source (Zhu et al., 2013), instead of conducting wavefield interaction involving

the memory variables. This method is derived from encoding the $Q$ information with the complex velocity (or modulus, Aki and Richards, 2002), and has been applied to the real VSP dataset for velocity/attenuation inversion (Pan and Innanen, 2019). Although the dispersion and dissipation terms are separated in the $Q$ adjoint source, it is still unclear how each of the decoupled terms contributes to the Fréchet kernel. Third, the coupling between elastic (velocity) and anelastic (attenuation) model parameters gives rise to the crosstalk artifacts (Kamei and Pratt, 2013; Keating and Innanen, 2019), which causes difficulties to determine whether the data residual should be attributed to velocity or attenuation.

Recently, a variety of viscoacoustic/viscoelastic wave equations featuring the fractional Laplacian operators (Chen and Holm, 2004) have been proposed for seismic modeling (e.g., Zhu and Harris, 2014; Zhu and Carcione, 2014; Chen et al., 2016; Xing and Zhu, 2019) as well as inversion (e.g., Chen et al., 2017, 2020; Yang et al., 2020). Their unique features suggest the potential to deal with the aforementioned issues in the $Q$-FWI. First, both forward and inversion algorithms based on these fractional equations fundamentally differ from the traditional methods: the traditional methods manage the attenuation effects through exploiting the temporal wavefield history by either storing it (e.g., Carcione et al., 2002; Zhu, 2017) or introducing memory variables to "record" the necessary part of it (e.g., Carcione et al., 1988; Fichtner and van Driel, 2014; Yang et al., 2016); while the algorithms based on the fractional equations retrieve the attenuation fingerprints embedded in the spatial variation of the wavefield. Second, these fractional equations, derived from the Kjartansson model that analytically characterizes the constant-$Q$ property (Kjartansson, 1979), have explicit representation of $Q$, instead of the implicit $Q$ parameterization using relaxation times of rheological mechanisms. Third, this type of equations has an exceptional characteristic that they decouple the attenuation-associated effects, i.e., dissipation and

dispersion, from the lossless wave propagation, with separate operators for different physical processes (Zhu, 2014). Previous studies showed that the decoupled operators enable the $Q$-compensated reverse-time migration and time-reversal imaging by only flipping the sign of the dissipation operator (Zhu, 2014; Zhu et al., 2014). Xue et al. (2018) demonstrated that the $Q$-compensated velocity FWI can accelerate the convergence, where both forward and adjoint simulations are compensated. This compensation acts as a preconditioner in the FWI to balance the illumination by boosting the gradient at depth that suffers from the "double-damping" (attenuated for both source-side and receiver-side wavefields), especially for the reflection acquisition system.

Taking advantage of these features, in this study, we provide a detailed derivation of the formulation for the Fréchet kernel computation based on a decoupled fractional viscoacoustic wave equation (Xing and Zhu, 2019), which improves the accuracy of simulating the wavefield in heterogeneous $Q$ media using fixed fractional Laplacian powers. As with the wave propagator that is decoupled into lossless propagation, dispersion, and dissipation operators, we demonstrate that the resultant Fréchet kernel can also be decoupled into contributions from these three physical processes, which could promote our understanding of the significance of each process in the $Q$-FWI. We also explore the Fréchet kernels of various misfit measurements (objective functions) to investigate its potential to disentangle the coupling between the velocity and attenuation.

We first introduce the forward modeling using the fractional viscoacoustic wave equation derived from the Kjartansson constant-$Q$ model. In the next section, we formulate its associated adjoint wave propagator and the Fréchet kernel computation for various misfit measurements. In the numerical example section, we conduct experiments to validate the kernel computation algorithm, and demonstrate the decoupling property and the sen-

sitivities of velocity/attenuation anomalies of the kernels. Meanwhile, the advantages and challenges of this algorithm are discussed, followed by presenting the conclusions.

## FORWARD MODELING

The Kjartansson model represents frequency-independent-$Q$ media with only three parameters (Kjartansson, 1979): the reference angular frequency $\omega_0$, its corresponding phase velocity $c_0$, and a dimensionless parameter $\gamma = \frac{1}{\pi} arctan(\frac{1}{Q})$ that represents the strength of attenuation. Based on this model, Xing and Zhu (2019) proposed a viscoacoustic wave equation featured by the fractional Laplacian operators:

$$\mathbf{L}u = (\mathbf{L_0} + \mathbf{L_1} + \mathbf{L_2})u = f, \tag{1}$$

$$\mathbf{L_0} = \frac{1}{c^2}\frac{\partial^2}{\partial t^2} - \nabla^2, \tag{2}$$

$$\mathbf{L_1} = -\gamma\frac{\omega_0}{c}(-\nabla^2)^{\frac{1}{2}} + \gamma\frac{c}{\omega_0}(-\nabla^2)^{\frac{3}{2}}, \tag{3}$$

$$\mathbf{L_2} = (\pi\gamma\frac{1}{c}(-\nabla^2)^{\frac{1}{2}} - \pi\gamma^2\frac{1}{\omega_0}\nabla^2)\frac{\partial}{\partial t}, \tag{4}$$

where $u$ is the pressure wavefield, $f$ is the source term, and $c = c_0 cos(\frac{\pi\gamma}{2})$ is the "propagation velocity". As shown in Equation (1), the viscoacoustic wave propagator $\mathbf{L}$ is decoupled into three parts: $\mathbf{L_0}$ the lossless acoustic wave propagator, $\mathbf{L_1}$ the phase dispersion corrector, and $\mathbf{L_2}$ the amplitude loss (dissipation) corrector. Each operator corresponds to a unique physical process. This equation characterizes the attenuation features by interrogating the spatial variation of the wavefield via operators $\mathbf{L_1}$ and $\mathbf{L_2}$. To numerically implement Equations (1-4), we follow Xing and Zhu (2019) to use the pseudospectral method to model the viscoacoustic wavefield with good accuracy and efficiency. Note that to guarantee the accuracy of the numerical simulation, the reference angular frequency $\omega_0$ should be selected, without loss of generality, to be the center of the frequency band of interest,

and the corresponding phase velocity $c_0$ should thus be adjusted accordingly based on the velocity dispersion of the Kjartansson model.

## FRÉCHET KERNELS

Following the Lagrangian multiplier method (Plessix, 2006), we can formulate the computation of Fréchet kernel $K$ with Equation (1) for forward modeling, and two extra equations for adjoint modeling and wavefield interaction, respectively:

$$\mathbf{L}^*\lambda = a = \frac{\partial \chi}{\partial u}, \tag{5}$$

$$K = \frac{d\chi}{dm} = -\langle \lambda, \frac{\partial \mathbf{L}}{\partial m} u \rangle, \tag{6}$$

where $*$ denotes adjoint, $\lambda$ is the adjoint wavefield, $\chi$ is the objective function, $a = \frac{\partial \chi}{\partial u}$ is the adjoint source, and $m$ is the model parameter. The inner (dot) product $\langle \cdot, \cdot \rangle$ of two wavefields $u$ and $v$ is defined by

$$\langle u, v \rangle = \int_0^T \int_V u(x,t) v(x,t) dx dt, \tag{7}$$

where $[0, T]$ and $V$ are the duration and the region of simulation, respectively. We will illustrate how to use both Equations (5) and (6) in the following subsections.

### Adjoint wave propagator $\mathbf{L}^*$

In order to use Equation (5), we need to derive the explicit form of $\mathbf{L}^* = \mathbf{L_0^*} + \mathbf{L_1^*} + \mathbf{L_2^*}$. For an arbitrary operator $\mathbf{P}$, its adjoint operator $\mathbf{P}^*$ satisfies $\langle \mathbf{P}u, v \rangle = \langle u, \mathbf{P}^* v \rangle$. As we have known that $(\nabla^2)^* = \nabla^2$ and $(\frac{\partial}{\partial t})^* = -\frac{\partial}{\partial t}$, we can infer from Equation (2) that the acoustic propagator is self-adjoint: $\mathbf{L_0^*} = \mathbf{L_0}$. For the fractional Laplacian operators $(-\nabla^2)^{\frac{1}{2}}$ and $(-\nabla^2)^{\frac{3}{2}}$, there is a lack of mathematical proof of their self-adjoint property. In the following,

we conduct dot product tests to numerically prove that both of these fractional Laplacian operators are self-adjoint.

The fractional Laplacians are spatial operators, so we just need to consider the dot product in only one single time slice without the time integral in Equation (7). Thus, we investigate two randomly generated single-time-slice wavefields $u$ (Figure 1a) and $v$ (Figure 1b). We apply fractional Laplacians (both $\frac{1}{2}$ and $\frac{3}{2}$ orders) to $u$ and $v$, and obtain the wavefields $(-\nabla^2)^{\frac{1}{2}}u$ (Figure 1c), $(-\nabla^2)^{\frac{1}{2}}v$ (Figure 1d), $(-\nabla^2)^{\frac{3}{2}}u$ (Figure 1e), and $(-\nabla^2)^{\frac{3}{2}}v$ (Figure 1f). Next, we conduct element-by-element multiplications between $(-\nabla^2)^{\frac{1}{2}}u$ (Figure 1c) and $v$ (Figure 1b) to obtain Figure 1(g), and between $(-\nabla^2)^{\frac{1}{2}}v$ (Figure 1d) and $u$ (Figure 1a) to get Figure 1(h). While these two resultant wavefields involving $\frac{1}{2}$ order Laplacians (Figures 1g and h) appear to be correlated but different, the summation of all the elements in each wavefield, i.e., the inner product, turns out to be the same (0.18). Similarly, we conduct the element-by-element multiplication and summation over elements for the $\frac{3}{2}$ order Laplacians, and obtain the equivalence (1.97) between $\langle(-\nabla^2)^{\frac{3}{2}}u, v\rangle$ (Figure 1i) and $\langle u, (-\nabla^2)^{\frac{3}{2}}v\rangle$ (Figure 1j). Hence, for this random wavefield pair ($u$ and $v$), we have $\langle(-\nabla^2)^{\frac{1}{2}}u, v\rangle = \langle u, (-\nabla^2)^{\frac{1}{2}}v\rangle$ and $\langle(-\nabla^2)^{\frac{3}{2}}u, v\rangle = \langle u, (-\nabla^2)^{\frac{3}{2}}v\rangle$. Moreover, we conduct tests for another 100 random wavefield pairs, and the comparisons of the resultant inner products are shown in Figure 2. Since the inner products are equivalent for each wavefield pair, we can conclude that both fractional Laplacian operators are self-adjoint: $((-\nabla^2)^{\frac{1}{2}})^* = (-\nabla^2)^{\frac{1}{2}}$ and $((-\nabla^2)^{\frac{3}{2}})^* = (-\nabla^2)^{\frac{3}{2}}$.

Hence, based on Equations (3) and (4), we have $\mathbf{L_1^*} = \mathbf{L_1}$ and $\mathbf{L_2^*} = -\mathbf{L_2}$, and thus $\mathbf{L}^* = \mathbf{L_0} + \mathbf{L_1} - \mathbf{L_2}$. Physically, it means that the adjoint viscoacoustic propagator compensates (anti-attenuates) the amplitude of the waves while preserves the velocity dispersion character (Zhu, 2014; Zhu et al., 2014). This behavior is consistent with the equations based

on the traditional "temporal-history" method, where Tarantola (1988) derived the adjoint wave equation and highlighted its feature of an "anti-causal" relaxation function that leads to the growth of energy (Komatitsch et al., 2016).

Contrary to the zero initial condition for forward modeling (Equation 1), the adjoint wave equation (Equation 5) is associated with a zero final (terminal) condition (Plessix, 2006). Hence, in practice, we simulate the adjoint wavefield in a time-reversed mode:

$$(\mathbf{L}^*)^\ddagger \lambda^\ddagger = a^\ddagger,$$

where $\ddagger$ indicates the time reversal. For variables (i.e., the adjoint wavefield $\lambda$ and the adjoint source $a$), the $\ddagger$ operator flips the time order; for operators (i.e., the adjoint viscoacoustic propagator $\mathbf{L}^*$ as well as its constituent $\mathbf{L_0^*}$, $\mathbf{L_1^*}$ and $\mathbf{L_2^*}$), it replaces $t$ with $-t$. As a result, we have $(\mathbf{L_0^*})^\ddagger = \mathbf{L_0^\ddagger} = \mathbf{L_0}$, $(\mathbf{L_1^*})^\ddagger = \mathbf{L_1^\ddagger} = \mathbf{L_1}$, and $(\mathbf{L_2^*})^\ddagger = -\mathbf{L_2^\ddagger} = \mathbf{L_2}$, and thus, straightforwardly, the time-reversed adjoint viscoacoustic propagator $(\mathbf{L}^*)^\ddagger = \mathbf{L_0}+\mathbf{L_1}+\mathbf{L_2} = \mathbf{L}$. Hence, instead of compensating, the time-reversed adjoint wavefield attenuates the amplitude and preserves the velocity dispersion as the forward wavefield:

$$\mathbf{L}\lambda^\ddagger = a^\ddagger. \tag{8}$$

In other words, the behavior of the time-reversed adjoint wave propagation is identical to that of the forward wavefield. Note that this invariance should be satisfied as long as the source-receiver reciprocity holds (Pratt et al., 1998).

### Adjoint source $\frac{\partial \chi}{\partial u}$

The right-hand side of Equation (5) suggests that the adjoint source exciting the adjoint wavefield depends on the form of the objective function $\chi$, which is the measurement of

the misfit between observed and synthetic seismograms. In the classic FWI, the waveform misfit is adopted as the objective function:

$$\chi_W = \frac{1}{2}\int (u-d)^2 dt, \tag{9}$$

where $u$ and $d$ are the synthetic and the observed seismograms, respectively. For simplicity, we consider the single-source single-receiver case; and we hereinafter omit the sampling operator at the receiver location, and the time window in which the measurement is conducted. Hence, its corresponding adjoint source is the data (waveform) residual, expressed as:

$$a_W = \frac{\partial \chi_W}{\partial u} = u - d. \tag{10}$$

Besides, we consider two additional objective functions, i.e., the cross-correlation traveltime shift and the amplitude difference. The traveltime objective function is defined by

$$\chi_T = \frac{1}{2}\Delta T^2 \qquad (\Delta T = T_u - T_d), \tag{11}$$

where $T_u$ and $T_d$ are the traveltimes of the synthetic and the observed seismograms, respectively; and the traveltime shift $\Delta T$ is defined by the time lag with the maximum cross-correlation coefficient of $u$ and $d$. Using the implicit differentiation technique (Luo and Schuster, 1991; Tromp et al., 2005), we can formulate the adjoint source for the traveltime objective function:

$$a_T = \frac{\partial \chi_T}{\partial u} = -\Delta T \frac{\dot{d}(t-\Delta T)}{\int \dot{u}(t)\dot{d}(t-\Delta T)dt}, \tag{12}$$

where the dot (in $\dot{d}$ and $\dot{u}$) denotes time derivative.

We can define the amplitude objective function as

$$\chi_A = \frac{1}{2}\Delta A^2 \qquad (\Delta A = \frac{A_u - A_d}{A_d}), \tag{13}$$

where $A_u = (\int u^2 dt)^{\frac{1}{2}}$ and $A_d = (\int d^2 dt)^{\frac{1}{2}}$ are the root-mean-square amplitudes of the synthetic and the observed seismograms, respectively. Its corresponding adjoint source can then be formulated (Dahlen and Baig, 2002; Tromp et al., 2005):

$$a_A = \frac{\partial \chi_A}{\partial u} = \Delta A \cdot \frac{u}{A_u A_d}. \tag{14}$$

In practice, the amplitude information could be unreliable when the signal-to-noise ratio is low. In such scenarios, other amplitude-based objective functions such as spectral amplitude ratio can also be considered (Pan and Innanen, 2019; Pan and Wang, 2020).

Generally, the traveltime and the amplitude captures the kinematic and the dynamic information, respectively. We incorporate these two misfit measurements as an attempt to understand the sensitivity of traveltime and amplitude data to velocity and attenuation.

### Wavefield interaction

The last step to compute the Fréchet kernel is to interact the forward and adjoint wavefields, which requires an explicit formulation of equation (6). As mentioned in Forward Modeling section, one of the unique features of the fractional wave equation is its capability to decouple the wave propagator $\mathbf{L}$ into three parts representing different physical processes: the lossless propagator $\mathbf{L_0}$, the dispersion corrector $\mathbf{L_1}$, and the dissipation corrector $\mathbf{L_2}$. As a result, the Fréchet kernel $K$ is perfectly separated into three parts as $\mathbf{L}$ does:

$$K = K_0 + K_1 + K_2 \qquad \text{where } K_i = -\langle \lambda, \frac{\partial \mathbf{L_i}}{\partial m} u \rangle \qquad (i = 0, 1, 2). \tag{15}$$

Here, we regard $c$ (propagation velocity) and $\gamma$ (attenuation strength, $\sim 1/\pi Q$) as the model parameters. Then the operators $\frac{\partial \mathbf{L_i}}{\partial m}$ can be derived directly from Equations (2)-(4), and

thus the decoupled Fréchet kernels can be obtained by:

$$K_{c,0} = -\langle \lambda, \frac{\partial \mathbf{L_0}}{\partial c} u \rangle = -\langle \lambda, -\frac{2}{c^3} \frac{\partial^2}{\partial t^2} u \rangle, \tag{16}$$

$$K_{c,1} = -\langle \lambda, \frac{\partial \mathbf{L_1}}{\partial c} u \rangle = -\langle \lambda, (\frac{\gamma \omega_0}{c^2} (-\nabla^2)^{\frac{1}{2}} + \frac{\gamma}{\omega_0} (-\nabla^2)^{\frac{3}{2}}) u \rangle, \tag{17}$$

$$K_{c,2} = -\langle \lambda, \frac{\partial \mathbf{L_2}}{\partial c} u \rangle = -\langle \lambda, -\frac{\pi \gamma}{c^2} (-\nabla^2)^{\frac{1}{2}} \frac{\partial}{\partial t} u \rangle, \tag{18}$$

$$K_{\gamma,0} = -\langle \lambda, \frac{\partial \mathbf{L_0}}{\partial \gamma} u \rangle = 0, \tag{19}$$

$$K_{\gamma,1} = -\langle \lambda, \frac{\partial \mathbf{L_1}}{\partial \gamma} u \rangle = -\langle \lambda, (-\frac{\omega_0}{c} (-\nabla^2)^{\frac{1}{2}} + \frac{c}{\omega_0} (-\nabla^2)^{\frac{3}{2}}) u \rangle, \tag{20}$$

$$K_{\gamma,2} = -\langle \lambda, \frac{\partial \mathbf{L_2}}{\partial \gamma} u \rangle = -\langle \lambda, (\frac{\pi}{c} (-\nabla^2)^{\frac{1}{2}} - \frac{2\pi\gamma}{\omega_0} \nabla^2) \frac{\partial}{\partial t} u \rangle. \tag{21}$$

Thus, we have decoupled the Fréchet kernels into contributions from three different physical processes: lossless propagation kernel $K_0$ (Equations 16 and 19), dispersion kernel $K_1$ (Equations 17 and 20), and dissipation kernel $K_2$ (Equations 18 and 21). Note that the form of Equation (16) is identical to the velocity gradient computation in the classic acoustic FWI (e.g., Bunks et al., 1995). Taking $K_{c,0}$ as an example (Equation 16), its physical meaning is: how significant the misfit will change due to the velocity ($c$) perturbation when only the lossless propagation process is considered. According to the Kjartansson model ($c$ is involved in both $\mathbf{L_1}$ and $\mathbf{L_2}$), the velocity perturbation will slightly affect the dispersion and the dissipation. The velocity kernel contributions from these two processes (Equations 17 and 18) are expected to be far less significant than the lossless propagation (Equation 16). Equation (19) indicates that the misfit will not change at all no matter how we manipulate the attenuation ($\gamma$) in a lossless world, thus the lossless propagation will not contribute to the attenuation kernel. In addition to the dispersion contribution (Equation 20), we would expect the attenuation to have a significant impact through the dissipation (Equation 21) process, which will be demonstrated in the Numerical Examples section.

## NUMERICAL EXAMPLES

### Kernel gallery

We implement the adjoint-state method derived in the previous section to compute the Fréchet kernels of a homogeneous model for three different objective functions. To do that, we consider a case of exploration scale, and set up a 2-D homogeneous target model on a $401 \times 201$ grid with spacing of 10 m in both directions. The target model has the reference phase velocity 3.05 km/s at 20 Hz and the quality factor $Q = 80$. We put a receiver at (3.7, 1) km and a source at (0.3, 1) km with a 20 Hz Ricker wavelet. We run the simulation with 1 ms time interval, and the resultant synthetic seismogram is regarded as the ground truth data.

Meanwhile, we set up an initial model on the same grid with 3 km/s reference phase velocity and $Q = 100$. Using this model, first, we simulate the forward wavefield according to Equation (1). Next, the synthetic recorded at the receiver is compared with the ground truth data to generate the adjoint sources for different objective functions according to Equations (10), (12), and (14). After that, the adjoint wavefield excited by each adjoint source is modeled in a time-reversed mode using the same simulator as the forward wavefield (Equation 8). Finally, the forward and the adjoint wavefields are interacted following Equations (16)-(21) to produce the Fréchet kernels contributed by different physical processes as well as their summation. The resultant velocity and attenuation kernels ($K_c$ and $K_\gamma$) are displayed in Figures 3 and 4, respectively.

Figure 3 and Figure 4 show the velocity and attenuation Fréchet kernels, respectively, for the three objective functions (waveform: $K_{c,W}$ and $K_{\gamma,W}$; traveltime: $K_{c,T}$ and $K_{\gamma,T}$; amplitude: $K_{c,A}$ and $K_{\gamma,A}$). In both figures, the first three rows are the decoupled kernels,

i.e., the contributions from lossless propagation ($K_0$), dispersion ($K_1$), and dissipation ($K_2$), respectively, while the bottom row is their summation ($K$, i.e., $K_{total}$). As expected, for all the objective functions, the velocity kernels ($K_c$, row 4 of Figure 3) are dominated by the contribution of lossless propagation ($K_{c,0}$ in Equation 16 and row 1 of Figure 3), while the dispersion and dissipation counterparts ($K_{c,1}$ in Equation 17 and $K_{c,2}$ in Equation 18) are very small and virtually invisible ($K_{c,1}$ in row 2, and $K_{c,2}$ in row 3 of Figure 3). On the contrary, the attenuation has absolutely no sensitivity of the lossless process ($K_{\gamma,0}$ in Equation 19 and row 1 of Figure 4), but is instead determined by the dispersion ($K_{\gamma,1}$ in Equation 20 and row 2 of Figure 4) and dissipation ($K_{\gamma,2}$ in Equation 21 and row 3 of Figure 4). While the dispersion kernel ($K_{\gamma,1}$) is relatively small, the dissipation kernel ($K_{\gamma,2}$ in Equation 21 and row 3 of Figure 4) is much larger for each of the objective functions.

To further quantify the kernel contribution from different processes (at least to some extent), we extract the central vertical profile (at 2 km of the horizontal coordinate) for each kernel and show them in Figure 5. The above observations can be confirmed: lossless propagation kernel $K_0$ dominates the velocity kernel, while the dissipation kernel $K_2$ contributes to the majority of the attenuation kernel. In addition, we noticed that the dispersion and dissipation attenuation kernels ($K_{\gamma,1}$ and $K_{\gamma,2}$) mildly anti-correlate with each other (correlation coefficients are -0.31, -0.54, and -0.11 for the three objective functions, respectively), as shown in the row 2 of Figure 5. We also extract the value at the central depth for each profile (i.e., the central point of the 2-D model), and present the percentage of the contributions from different processes in Table 1. It turns out that the lossless propagation ($K_0$) contributes almost 100% of the velocity kernel; while the dissipation ($K_2$) is dominant by taking up more than 80% of the attenuation kernel, compared to the dispersion ($K_1$) contribution, which is around 20%.

Since the target model has higher velocity compared to the initial model, we would expect that the majority of the velocity kernel to be negative. In this sense, the traveltime kernel ($K_{c,T}$ in Figure 3) with the largest bluish area is more likely to benefit the FWI convergence compared to the others. On the other hand, the target model also has higher attenuation (lower $Q$), which is well captured by both the waveform and the amplitude kernels ($K_{\gamma,A}$ in Figure 4) with negative values in the Fresnel zone. The traveltime attenuation kernel ($K_{\gamma,T}$ in Figure 4), however, has a flipped polarity. As the attenuation is barely sensitive to the traveltime phase shift, the traveltime attenuation kernel generally should not be used to update the model.

It is worth mentioning that the raw kernels, especially the attenuation kernels, have a cross-shaped artifact near the source location. For example, a part (boxed area of Figure 4j) of the raw waveform attenuation kernel is shown in Figure 6(a). This artifact is produced by applying fractional Laplacian operators on the source-point singularity when the wavefield interaction is taken (Equations 17, 18, 20, and 21). To suppress the artifact, we use a Gaussian function to taper the source region of the forward wavefield for all the time steps before the wavefield interaction. With this source region taper (SRT) process, the attenuation kernel is shown in Figure 6(b), and the cross-shaped artifact disappears. By checking the difference between the kernels with and without SRT (Figure 6c), we can see that the artifact is mostly removed along with the kernel of a small source region. Since the model parameters are not updated at the source region in practice, this SRT solution for the artifact is valid. All the Fréchet kernels in Figures 3 and 4 are generated with SRT.

### Finite-difference validation

To validate our algorithm, in this subsection, we use the finite-difference (FD) method to compute the kernels of a small (61 $\times$ 31) model, and compare them with the ones obtained by the adjoint-state (AD) method. Apart from the size, the setup of the target and initial models are the same as the previous section. The source and the receiver are located at (0.10, 0.15) km and (0.50, 0.15) km, respectively. The AD kernels are computed as illustrated in the previous section but without SRT (for better validation).

Based on Equation (6), the FD Fréchet kernel $\tilde{K}$ can be defined by

$$\tilde{K} = \frac{\Delta\chi}{\Delta m} \approx \frac{d\chi}{dm}, \tag{22}$$

when the model parameter perturbation $\Delta m$ is sufficiently small. To implement, we first compute the original objective function, which is the misfit between the observed data and the synthetic seismogram generated by the initial model. For one single grid point of the initial model, we perturb the parameter by a small value $\Delta m$ (1 km/s for velocity $\Delta c$, $10^{-3}$ for attenuation $\Delta\gamma$). Using this perturbed model, we simulate the new synthetic and compute the perturbed objective function, which has a subtle difference $\Delta\chi$ compared to the original objective function. The FD Fréchet kernel value at this grid point is then set to be $\frac{\Delta\chi}{\Delta m}$, followed by undoing the perturbation $\Delta m$. We iterate this process for all the grid points in the model to obtain the FD Fréchet kernel $\tilde{K}$.

The comparison between the AD kernels and the FD kernels is shown in Figure 7. Here, we only show the kernels for the waveform and the amplitude misfit, because the tiny traveltime change caused by the perturbation of one grid point cannot be measured by the cross-correlation method, which results in zero traveltime FD kernels. It turns out that the kernels generated by both methods are consistent with each other. For each

objective function, there is some residual near the source location (Column 3 of Figure 7) because of its singularity. Apart from that, the velocity kernel residuals are negligible. The visible residuals of the attenuation kernels are because the attenuation perturbation ($\Delta\gamma = 10^{-3}$, here corresponding to $\Delta Q = 23.9$) is not small enough to guarantee the accuracy of the approximation in Equation (22). However, if we decrease $\Delta\gamma$, the objective function perturbation $\Delta J$ will fall below the level of numerical noise, which leads to a noisy FD kernel. Nevertheless, we believe that the similarity between the attenuation AD and the FD kernels is fair enough to validate our adjoint-state method for Fréchet kernel computation.

### Circular anomaly model

In this subsection, we demonstrate the capability of Fréchet kernels with regarding to a velocity anomaly (Test 1) and an attenuation anomaly (Test 2). The initial model is the same homogeneous model as in the first numerical example. Compared to the initial model, the Test 1 target model has a circular (radius 0.3 km) velocity anomaly of 3.1 km/s centered at (1.5, 0.8) km. We have 56 sources (20 on top/bottom, 8 on left/right) and 118 receivers (40 on top/bottom, 19 on left/right) evenly distributed on the four margins of the model. As in the previous examples, the sources are 20 Hz Ricker wavelet, and the simulations are ran with 1 ms time interval.

For each source, we compute the velocity and the attenuation Fréchet kernels for all the three objective functions, and show the ones generated by the source at (1.15, 0.15) km in Figures 8. The waveform ($K_{c,W}$) and the traveltime ($K_{c,T}$) have narrow fan-shaped velocity kernels that concentrated on the wave paths passing through the anomalous area, while the

amplitude kernel ($K_{c,A}$) is much wider with artifacts in adjacent zones. Besides, the stacked Fréchet kernels from all the sources are shown in Figure 9. It appears that velocity kernels of all the three objective functions (Figures 9a, c and e) reveal the velocity anomaly. In particular, the waveform kernel (Figure 9a) and the traveltime kernel (Figure 9c) better capture the interior of the anomaly; while the amplitude kernel (Figure 9e) emphasizes the boundary of the anomaly with larger contrasts. Meanwhile, the attenuation kernels (column 2 of Figures 8 and 9) indicate the crosstalk between velocity and attenuation.

Test 2 is conducted for a target model with a $Q = 50$ anomaly at the same anomaly location as Test 1, and a homogeneous velocity model. The resultant single-source and the stacked kernels are shown in Figures 10 and 11, respectively. As expected, the waveform ($K_{\gamma,W}$) and the amplitude ($K_{\gamma,A}$) attenuation kernels delineate the anomaly well (Figures 11b and f), while the traveltime ($K_{\gamma,T}$) has little sensitivity to the $Q$ variation (Figure 11d). The leakage to the incorrect parameter (velocity) also exists in this test as shown by the velocity kernels (the left column of Figures 10 and 11). Both tests in this subsection manifest the crosstalk between velocity and attenuation.

## DISCUSSION

This study aims to establish a new Fréchet kernel computation algorithm based on a fractional viscoacoustic wave equation, which may resolve the three issues of the $Q$-FWI: the implicit $Q$ parameterization, the dispersion-dissipation coupling, and the velocity-attenuation crosstalk. First, this wave equation, and thus the kernel computation, intrinsically involves the explicit $Q$ (parametrized as attenuation strength $\gamma$) as a coefficient. Thus it avoids implicit $Q$ representation (or the curve-fitting process) of rheological-mechanism-based methods (Fichtner and van Driel, 2014; Yang et al., 2016).

Second, the decoupled wave equation operators ($\mathbf{L_0}$, $\mathbf{L_1}$, and $\mathbf{L_2}$ in Equation 1) lead to the decoupled Fréchet kernels ($K_0$, $K_1$, and $K_2$ in Equations 16 - 21) that directly represent the contributions from different physical processes, i.e., the lossless propagation, the dispersion and the dissipation. The lossless propagation ($K_0$) dominates the velocity kernel, while the dissipation ($K_2$) dominates the attenuation kernel, which indicates the significance of each physical process in the $Q$-FWI. Taking advantage of it, we could save some computational cost by using $K_0$ as the velocity kernel, and $K_2$ as the attenuation kernel. In addition, as with the $Q$-compensated reverse-time migration (Zhu, 2014; Zhu et al., 2014; Xing and Zhu, 2019), the decoupling of the operators could also be used to construct the $Q$-compensated FWI algorithm (Xue et al., 2018), where both forward and time-reversed adjoint wavefields are compensated to boost the kernel below low-$Q$ areas.

Third, our derived formulation may provide an option to mitigate the crosstalk between velocity and attenuation by involving different misfit measurements other than the classic waveform residual (Pan and Wang, 2020). In particular, the traveltime dominated by the kinematic part of the data can well capture the interior of the velocity anomaly, but is hardly sensitive to attenuation; while the amplitude primarily representing the dynamic part highlights the boundary of the velocity anomaly, and is particularly suitable for attenuation inversion. Our formulation provides the flexibility to accommodate any misfit measurements by casting the adjoint source corresponding to the objective function (Equation 5), although the kernels of the three conventional misfits (waveform, traveltime, and amplitude) in the circular anomaly example show the crosstalk between the two parameter classes (both kinematic and dynamic information can be attributed to either velocity or attenuation after all). Potential solutions within the kernel-based (i.e., gradient-based) framework include involving more advanced misfit measurements such as the envelope (e.g., Bozdağ et al.,

2011), the peak frequency (e.g., Dutta and Schuster, 2016) or the spectral ratio (e.g., Pan and Wang, 2020). In addition, incorporating the second-order Fréchet derivative, i.e., the Hessian, might be a good option to mitigate the crosstalk artifacts (e.g., Operto et al., 2013; Yang et al., 2018; Xing and Zhu, 2020). The future work should be focused on investigating how to promote the performance of the multiparameter inversion, in particular how to make the most of kernels of different objective functions and how to incorporate the Hessian information.

Furthermore, we would like to mention that the derivation of the Fréchet kernels in this study is associated with a recently proposed viscoacoustic wave equation (Xing and Zhu, 2019). In fact, the kernels with respect to viscoelastic, anisotropic, and attenuation-anisotropic properties (e.g., $Q_s$, $\delta$, $\epsilon_Q$) can be further derived based on fractional wave equations incorporating viscoelasticity (Wang et al., 2019) and anisotropy (Zhu and Bai, 2019).

## CONCLUSIONS

We have established a new system of formulations to compute the velocity and the attenuation Fréchet kernels for different objective functions based on a fractional viscoacoustic wave equation. These Fréchet kernels lay the foundation of the $Q$-FWI with fractional formulation. We have numerically proved that both 1/2- and 3/2-order fractional Laplacian operators are self-adjoint, which facilitates the derivation of the adjoint viscoacoustic wave propagator: it preserves the phase dispersion while compensates the amplitude. In practice, however, the time-reversed adjoint wavefield behaves identically as the forward one with the same dispersion and dissipation characters. This new formulation presents an explicit $Q$ parameterization instead of the implicit one in traditional methods. The resultant Fréchet

kernels for both velocity and attenuation can be decoupled into $K_0$ the lossless propagation kernel, $K_1$ the dispersion kernel, and $K_2$ the dissipation kernel. We found that the lossless propagation kernel $K_0$ dominates the velocity kernel; while the dissipation $K_2$ dominates the attenuation kernel. Numerical experiments using different objective functions suggest that waveform and traveltime are sensitive to the interior of velocity anomaly while amplitude emphasizes its boundary; rather than the traveltime, the waveform and the amplitude misfits are more suitable for attenuation inversion.

## ACKNOWLEDGMENTS

This work was supported by the National Energy Technology Laboratory of the U.S. Department of Energy under the U.S. DOE Contract No. DE-FE0031544, and the National Science Foundation Grant EAR 1919650.

## REFERENCES


Aki, K., and P. Richards, 2002, Quantitative seismology: University Science Books. Geology (University Science Books).: Seismology.

Bai, J., D. Yingst, R. Bloor, and J. Leveille, 2014, Viscoacoustic waveform inversion of velocity structures in the time domain viscoacoustic waveform inversion: Geophysics, **79**, R103–R119.

Bozdağ, E., J. Trampert, and J. Tromp, 2011, Misfit functions for full waveform inversion based on instantaneous phase and envelope measurements: Geophysical Journal International, **185**, 845–870.

Bunks, C., F. M. Saleck, S. Zaleski, and G. Chavent, 1995, Multiscale seismic waveform inversion: Geophysics, **60**, 1457–1473.

Carcione, J. M., F. Cavallini, F. Mainardi, and A. Hanyga, 2002, Time-domain modeling of constant-$Q$ seismic waves using fractional derivatives: Pure and Applied Geophysics, **159**, 1719–1736.

Carcione, J. M., D. Kosloff, and R. Kosloff, 1988, Wave propagation simulation in a linear viscoelastic medium: Geophysical Journal International, **95**, 597–611.

Chen, H., H. Zhou, Q. Li, and Y. Wang, 2016, Two efficient modeling schemes for fractional Laplacian viscoacoustic wave equation: Geophysics, **81**, T233–T249.

Chen, H., H. Zhou, and Y. Rao, 2020, Source wavefield reconstruction in fractional laplacian viscoacoustic wave equation-based full waveform inversion: IEEE Transactions on Geoscience and Remote Sensing.

Chen, H., H. Zhou, and S. Zu, 2017, Simultaneous inversion of velocity and q using a fractional laplacian constant-q wave equation: 79th EAGE Conference and Exhibition 2017, European Association of Geoscientists & Engineers, 1–5.

Chen, W., and S. Holm, 2004, Fractional Laplacian time-space models for linear and nonlinear lossy media exhibiting arbitrary frequency power-law dependency: The Journal of the Acoustical Society of America, **115**, 1424–1430.

Dahlen, F., and A. M. Baig, 2002, Fréchet kernels for body-wave amplitudes: Geophysical Journal International, **150**, 440–466.

Dutta, G., and G. T. Schuster, 2016, Wave-equation q tomography: Geophysics, **81**, R471–R484.

Fichtner, A., 2010, Full seismic waveform modelling and inversion: Springer Science & Business Media.

Fichtner, A., and M. van Driel, 2014, Models and Fréchet kernels for frequency-(in) dependent $Q$: Geophysical Journal International, **198**, 1878–1889.

Kamei, R., and R. Pratt, 2013, Inversion strategies for visco-acoustic waveform inversion: Geophysical Journal International, **194**, 859–884.

Keating, S., and K. A. Innanen, 2019, Parameter crosstalk and modeling errors in viscoacoustic seismic full-waveform inversion: Geophysics, **84**, R641–R653.

Kjartansson, E., 1979, Constant $Q$-wave propagation and attenuation: Journal of Geophysical Research: Solid Earth, **84**, 4737–4748.

Knopoff, L., 1964, $Q$: Reviews of Geophysics, **2**, 625–660.

Komatitsch, D., Z. Xie, E. Bozdağ, E. Sales de Andrade, D. Peter, Q. Liu, and J. Tromp, 2016, Anelastic sensitivity kernels with parsimonious storage for adjoint tomography and full waveform inversion: Geophysical Journal International, **206**, 1467–1478.

Liu, Q., and Y. Gu, 2012, Seismic imaging: From classical to adjoint tomography: Tectonophysics, **566**, 31–66.

Luo, Y., and G. T. Schuster, 1991, Wave-equation traveltime inversion: Geophysics, **56**,

645–653.

McDonal, F., F. Angona, R. Mills, R. Sengbush, R. Van Nostrand, and J. White, 1958, Attenuation of shear and compressional waves in Pierre Shale: Geophysics, **23**, 421–439.

Müller, T. M., B. Gurevich, and M. Lebedev, 2010, Seismic wave attenuation and dispersion resulting from wave-induced flow in porous rocks—A review: Geophysics, **75**, 75A147–75A164.

Operto, S., Y. Gholami, V. Prieux, A. Ribodetti, R. Brossier, L. Metivier, and J. Virieux, 2013, A guided tour of multiparameter full-waveform inversion with multicomponent data: From theory to practice: The Leading Edge, **32**, 1040–1054.

Pan, W., and K. A. Innanen, 2019, Amplitude-based misfit functions in viscoelastic full-waveform inversion applied to walk-away vertical seismic profile data: Geophysics, **84**, B335–B351.

Pan, W., and Y. Wang, 2020, On the influence of different misfit functions for attenuation estimation in viscoelastic full-waveform inversion: synthetic study: Geophysical Journal International, **221**, 1292–1319.

Plessix, R.-E., 2006, A review of the adjoint-state method for computing the gradient of a functional with geophysical applications: Geophysical Journal International, **167**, 495–503.

Pratt, R. G., C. Shin, and G. Hick, 1998, Gauss–newton and full newton methods in frequency–space seismic waveform inversion: Geophysical Journal International, **133**, 341–362.

Romanowicz, B., 1995, A global tomographic model of shear attenuation in the upper mantle: Journal of Geophysical Research: Solid Earth, **100**, 12375–12394.

Tarantola, A., 1988, Theoretical background for the inversion of seismic waveforms, includ-

ing elasticity and attenuation, *in* Scattering and Attenuations of Seismic Waves, Part I: Springer, 365–399.

Tromp, J., C. Tape, and Q. Liu, 2005, Seismic tomography, adjoint methods, time reversal and banana-doughnut kernels: Geophysical Journal International, **160**, 195–216.

Virieux, J., and S. Operto, 2009, An overview of full-waveform inversion in exploration geophysics: Geophysics, **74**, WCC1–WCC26.

Wang, N., G. Xing, and T. Zhu, 2019, Accurately propagating p-and s-waves in attenuation media using spatial-independent-order decoupled fractional laplacians, *in* SEG Technical Program Expanded Abstracts 2019: Society of Exploration Geophysicists, 3805–3809.

Wiens, D. A., J. A. Conder, and U. H. Faul, 2008, The seismic structure and dynamics of the mantle wedge: Annu. Rev. Earth Planet. Sci., **36**, 421–455.

Xing, G., and T. Zhu, 2019, Modeling frequency-independent $Q$ viscoacoustic wave propagation in heterogeneous media: Journal of Geophysical Research: Solid Earth, **124**, 11568–11584.

———, 2020, Hessian-based multiparameter fractional viscoacoustic full waveform inversion, *in* SEG Technical Program Expanded Abstracts 2020: Society of Exploration Geophysicists, in press.

Xue, Z., J. Sun, S. Fomel, and T. Zhu, 2018, Accelerating full-waveform inversion with attenuation compensation: Geophysics, **83**, A13–A20.

Yang, J., H. Zhu, X. Li, L. Ren, and S. Zhang, 2020, Estimating p-wave velocity and attenuation structures using full waveform inversion based on a time-domain complex-valued viscoacoustic wave equation: The method: Journal of Geophysical Research: Solid Earth, **125**, e2019JB019129.

Yang, P., R. Brossier, L. Métivier, and J. Virieux, 2016, A review on the systematic formu-

lation of 3-D multiparameter full waveform inversion in viscoelastic medium: Geophysical Journal International, **207**, 129–149.

Yang, P., R. Brossier, L. Métivier, J. Virieux, and W. Zhou, 2018, A time-domain preconditioned truncated newton approach to visco-acoustic multiparameter full waveform inversion: SIAM Journal on Scientific Computing, **40**, B1101–B1130.

Zhu, H., E. Bozdağ, T. S. Duffy, and J. Tromp, 2013, Seismic attenuation beneath europe and the north atlantic: Implications for water in the mantle: Earth and Planetary Science Letters, **381**, 1–11.

Zhu, T., 2014, Time-reverse modelling of acoustic wave propagation in attenuating media: Geophysical Journal International, **197**, 483–494.

———, 2017, Numerical simulation of seismic wave propagation in viscoelastic-anisotropic media using frequency-independent $Q$ wave equation: Geophysics, **82**, WA1–WA10.

Zhu, T., J. B. Ajo-Franklin, and T. M. Daley, 2017, Spatiotemporal changes of seismic attenuation caused by injected $CO_2$ at the Frio-II pilot site, Dayton, TX, USA: Journal of Geophysical Research: Solid Earth, **122**, 7156–7171.

Zhu, T., and T. Bai, 2019, Efficient modeling of wave propagation in a vertical transversely isotropic attenuative medium based on fractional laplacian: Geophysics, **84**, T121–T131.

Zhu, T., and J. M. Carcione, 2014, Theory and modelling of constant-$Q$ P-and S-waves using fractional spatial derivatives: Geophysical Journal International, **196**, 1787–1795.

Zhu, T., and J. M. Harris, 2014, Modeling acoustic wave propagation in heterogeneous attenuating media using decoupled fractional laplacians: Geophysics, **79**, T105–T116.

Zhu, T., J. M. Harris, and B. Biondi, 2014, $Q$-compensated reverse-time migration: Geophysics, **79**, S77–S87.

## LIST OF TABLES

## LIST OF FIGURES

method and the finite-difference (FD) method. Column 1: AD kernels; Column 2: FD kernels; column 3: residual between the AD and the FD kernels. Row 1: waveform velocity kernel ($K_{c,W}$ and $\tilde{K}_{c,W}$); row 2: waveform attenuation kernel ($K_{\gamma,W}$ and $\tilde{K}_{\gamma,W}$); row 3: amplitude velocity kernel ($K_{c,A}$ and $\tilde{K}_{c,A}$); row 4: amplitude attenuation kernel ($K_{\gamma,A}$ and $\tilde{K}_{\gamma,A}$).

8 Single-source Fréchet kernels for the Test 1 (velocity-anomaly model). Column 1: velocity kernels ($K_c$); Column 2: attenuation kernels ($K_\gamma$). Row 1: waveform; row 2: traveltime; row 3: amplitude.

9 Stacked Fréchet kernels for the Test 1 (velocity-anomaly model). Column 1: velocity kernels ($K_c$); Column 2: attenuation kernels ($K_\gamma$). Row 1: waveform; row 2: traveltime; row 3: amplitude.

10 Single-source Fréchet kernels for the Test 2 (attenuation-anomaly model). Column 1: velocity kernels ($K_c$); Column 2: attenuation kernels ($K_\gamma$). Row 1: waveform; row 2: traveltime; row 3: amplitude.

11 Stacked Fréchet kernels for the Test 2 (attenuation-anomaly model). Column 1: velocity kernels ($K_c$); Column 2: attenuation kernels ($K_\gamma$). Row 1: waveform; row 2: traveltime; row 3: amplitude.

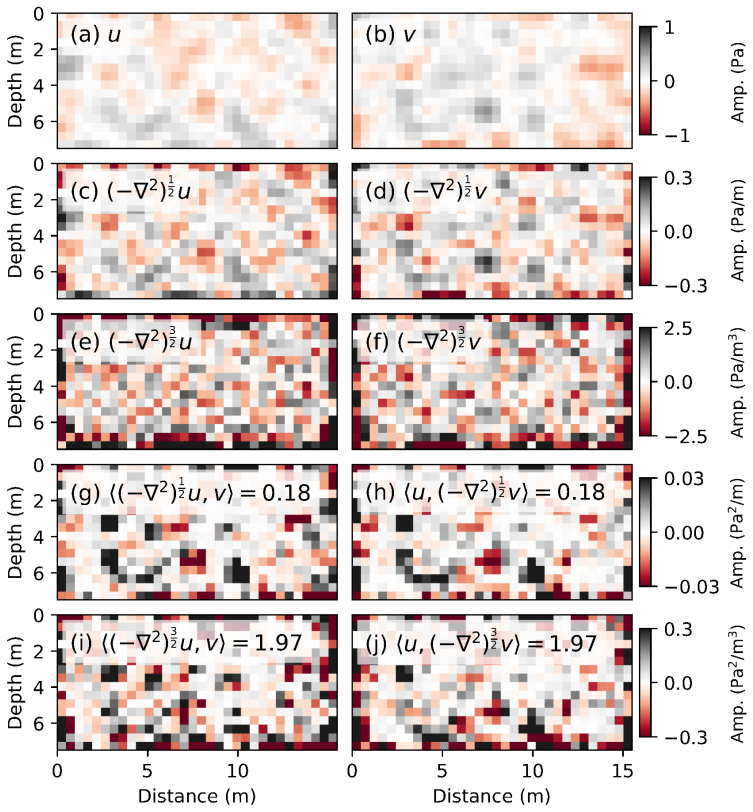


Figure 1: The dot product test of the fractional Laplacian operators for one random wavefield pair.

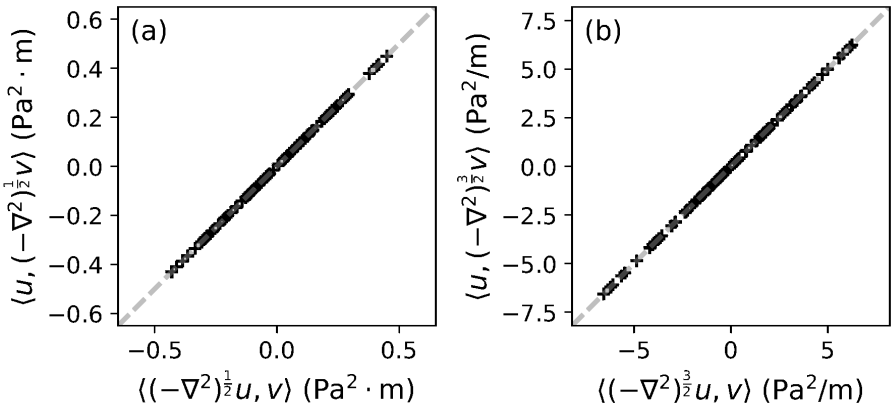


Figure 2: The dot product test results of 100 wavefield pairs for (a) $(-\nabla^2)^{\frac{1}{2}}$ and (b) $(-\nabla^2)^{\frac{3}{2}}$. Each black cross denotes the result of a wavefield pair; the gray dashed line shows where the values of x- and y-axis are equal.

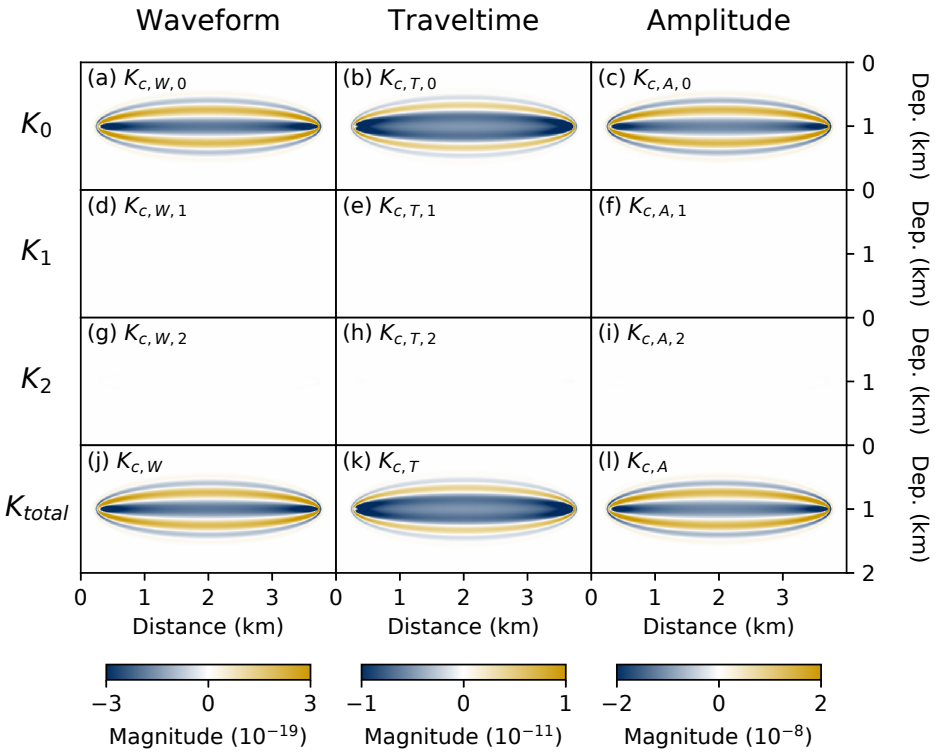


Figure 3: Velocity Fréchet kernels ($K_c$) for waveform (column 1), traveltime (column 2), and amplitude (column 3) objective functions. Row 1: $K_0$, contribution from the lossless propagation ($\mathbf{L_0}$); row 2: $K_1$, contribution from the dispersion ($\mathbf{L_1}$); row 3: $K_2$, contribution from the dissipation ($\mathbf{L_2}$); row 4: the total Fréchet kernels.

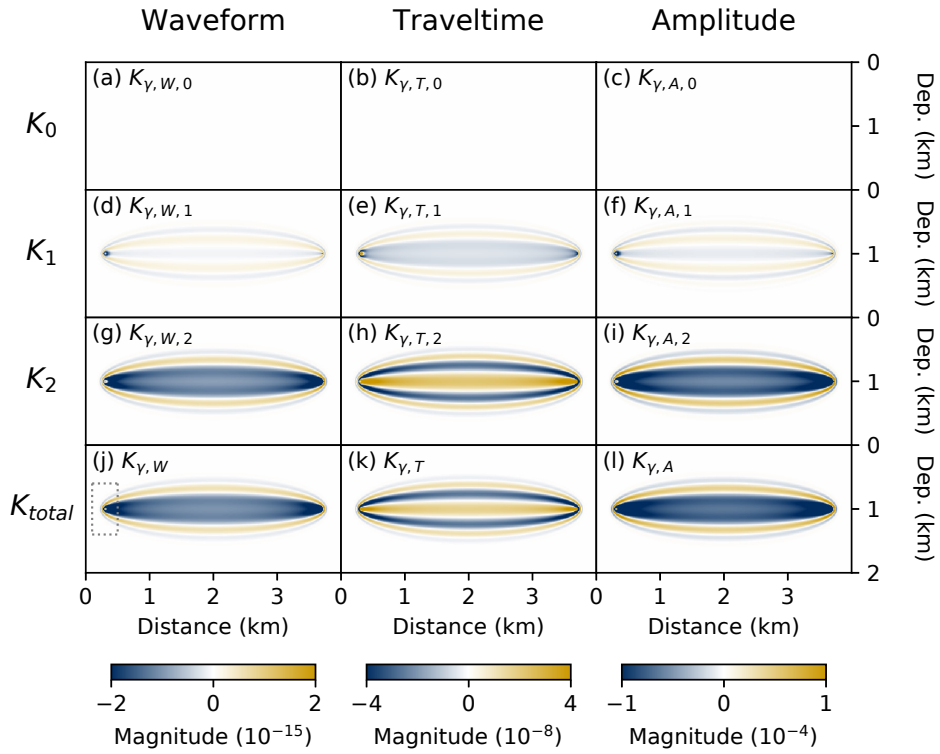


Figure 4: Attenuation Fréchet kernels ($K_\gamma$) for waveform (column 1), traveltime (column 2), and amplitude (column 3) objective functions. Row 1: $K_0$, contribution from the lossless propagation ($\mathbf{L_0}$); row 2: $K_1$, contribution from the dispersion ($\mathbf{L_1}$); row 3: $K_2$, contribution from the dissipation ($\mathbf{L_2}$); row 4: the total Fréchet kernels. The boxed area of (j) is used to illustrate the source region taper (SRT) process in Figure 6.

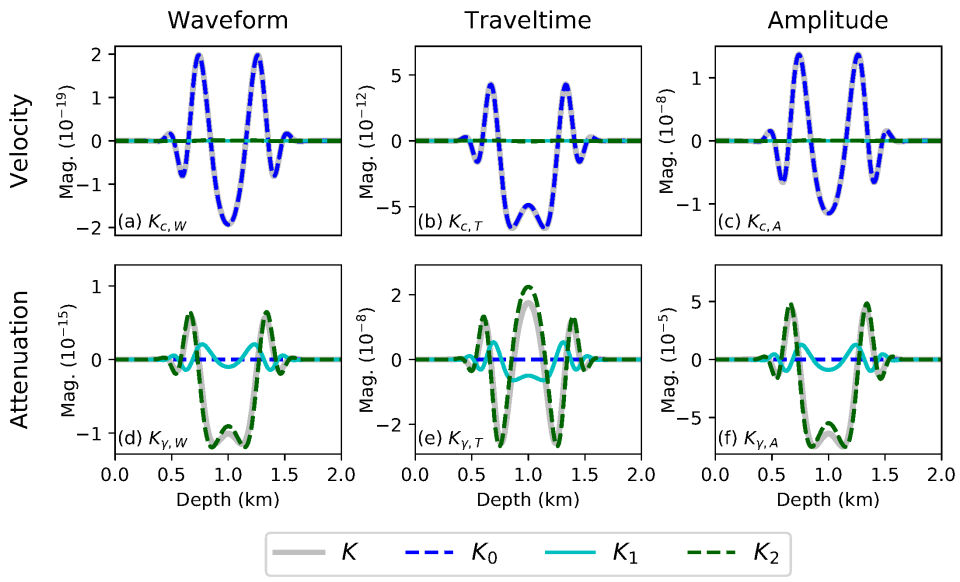


Figure 5: Central vertical profiles (at 2 km of the horizontal coordinate) of Fréchet kernels for waveform (column 1), traveltime (column 2), and amplitude (column 3) objective functions. Row 1: velocity kernel ($K_c$); row 2: attenuation kernel ($K_\gamma$). Gray solid line: total kernel $K$; blue dashed line: lossless propagation kernel ($K_0$); cyan solid line: dispersion kernel ($K_1$); green dashed line: dissipation kernel ($K_2$).

| | $K_{c,W}$ | $K_{c,T}$ | $K_{c,A}$ | $K_{\gamma,W}$ | $K_{\gamma,T}$ | $K_{\gamma,A}$ |
|---|---|---|---|---|---|---|
| Loss propagation $K_0$ | 100.17% | 99.17% | 100.17% | 0.00% | 0.00% | 0.00% |
| Dispersion $K_1$ | 0.14% | 0.12% | 0.13% | 10.02% | -28.40% | 14.07% |
| Dissipation $K_2$ | -0.30% | 0.71% | -0.29% | 89.98% | 128.40% | 85.93% |

Table 1: Kernel contributions from different operators at the central point of a homogeneous model

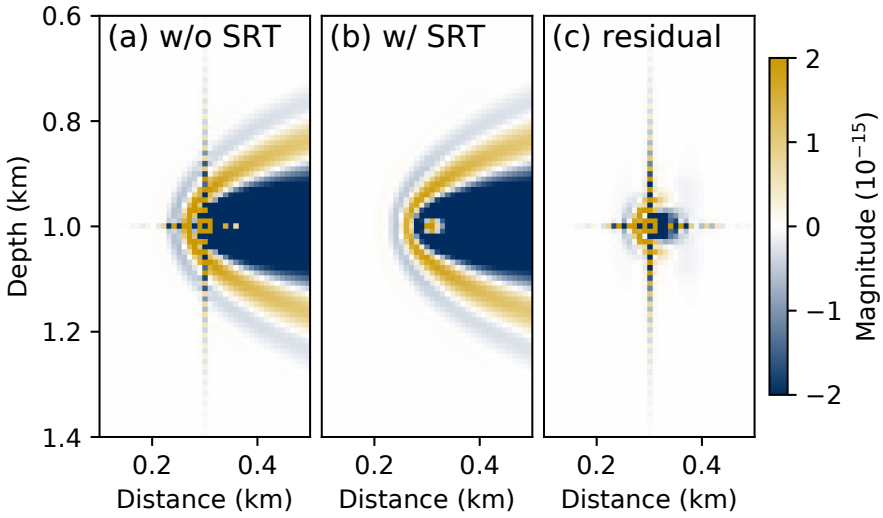


Figure 6: The effect of the source region taper (SRT). (a) The raw attenuation kernel without SRT; (b) the attenuation kernel with SRT (a close-up of the boxed area in Figure 4j); (c) the difference between the kernels with and without SRT.

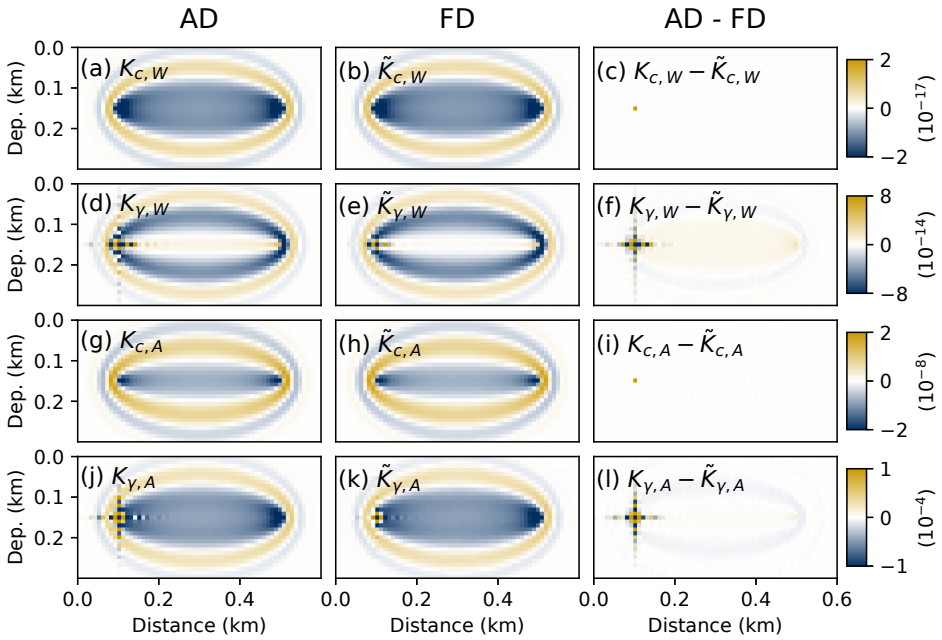


Figure 7: The comparison between Fréchet kernels computed using the adjoint-state (AD) method and the finite-difference (FD) method. Column 1: AD kernels; Column 2: FD kernels; column 3: residual between the AD and the FD kernels. Row 1: waveform velocity kernel ($K_{c,W}$ and $\tilde{K}_{c,W}$); row 2: waveform attenuation kernel ($K_{\gamma,W}$ and $\tilde{K}_{\gamma,W}$); row 3: amplitude velocity kernel ($K_{c,A}$ and $\tilde{K}_{c,A}$); row 4: amplitude attenuation kernel ($K_{\gamma,A}$ and $\tilde{K}_{\gamma,A}$).

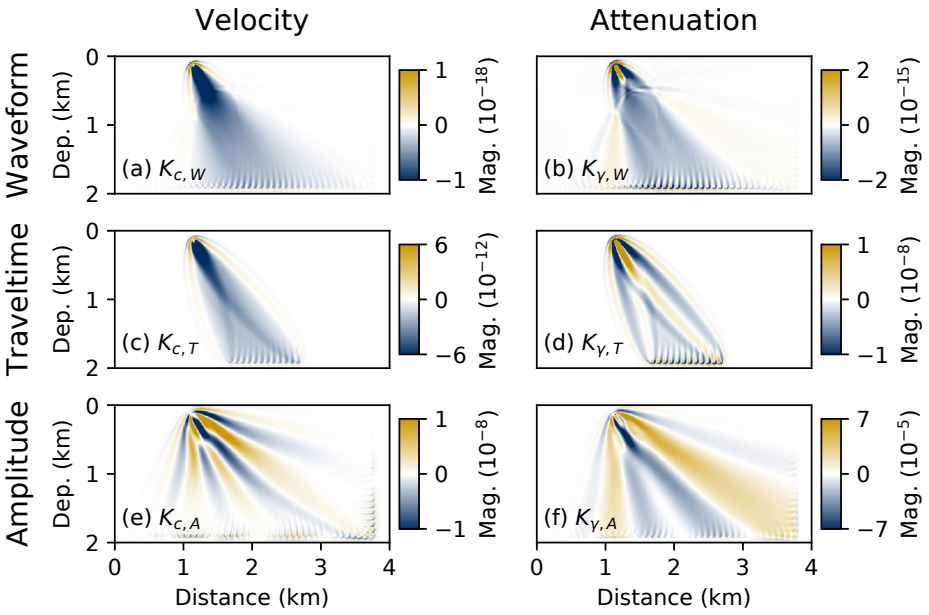


Figure 8: Single-source Fréchet kernels for the Test 1 (velocity-anomaly model). Column 1: velocity kernels ($K_c$); Column 2: attenuation kernels ($K_\gamma$). Row 1: waveform; row 2: traveltime; row 3: amplitude.

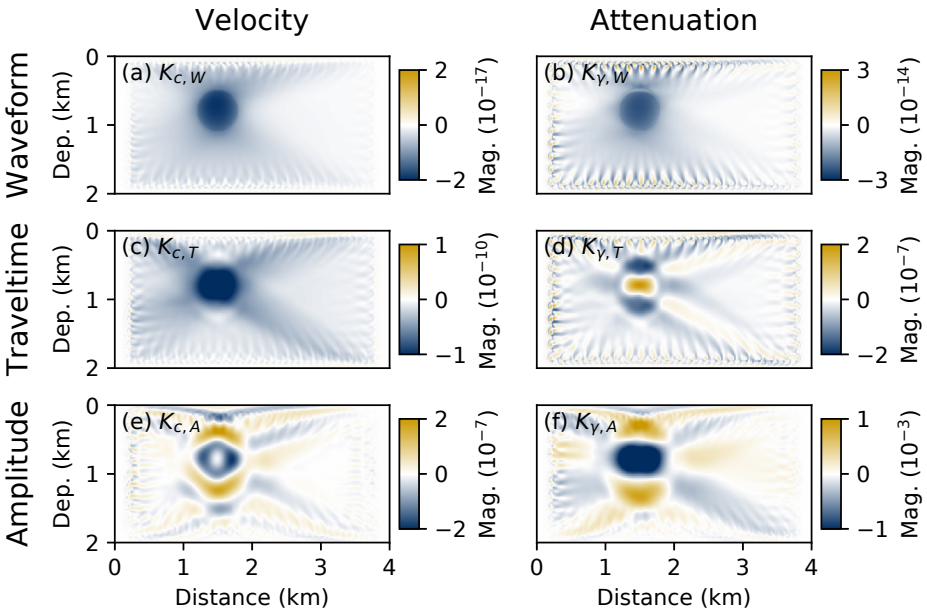


Figure 9: Stacked Fréchet kernels for the Test 1 (velocity-anomaly model). Column 1: velocity kernels ($K_c$); Column 2: attenuation kernels ($K_\gamma$). Row 1: waveform; row 2: traveltime; row 3: amplitude.

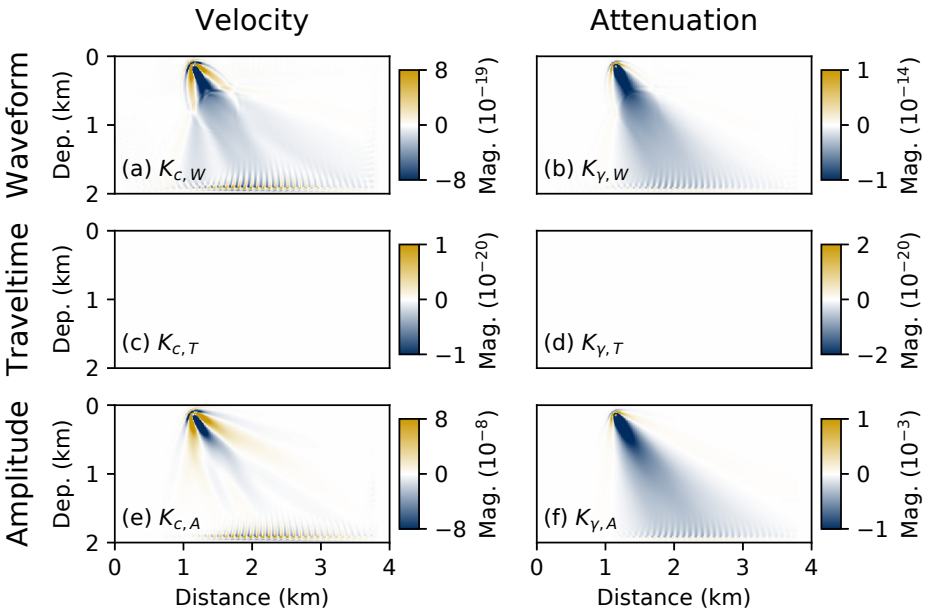


Figure 10: Single-source Fréchet kernels for the Test 2 (attenuation-anomaly model). Column 1: velocity kernels ($K_c$); Column 2: attenuation kernels ($K_\gamma$). Row 1: waveform; row 2: traveltime; row 3: amplitude.

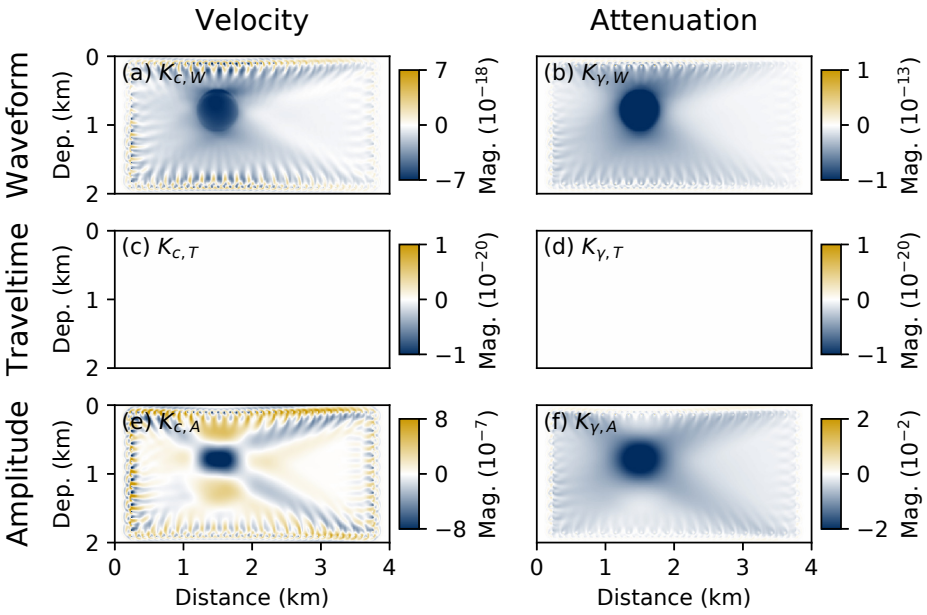


Figure 11: Stacked Fréchet kernels for the Test 2 (attenuation-anomaly model). Column 1: velocity kernels ($K_c$); Column 2: attenuation kernels ($K_\gamma$). Row 1: waveform; row 2: traveltime; row 3: amplitude.